Dedicated to the 100th anniversary of Chemistry at Nankai University

# Size-refinement enhanced flexibility and electrochemical performance of MXene electrodes for flexible waterproof supercapacitors

Jinkun Sun [a,b], Yingjian Liu [c], Jiayi Huang [a], Jiatian Li [a], Mengmeng Chen [a], Xiaoyu Hu [a], Yatao Liu [b], Run Wang [a], Yanan Shen [a], Jingjing Li [a], Xuecheng Chen [d,*], Dong Qian [c], Baigang An [b,*], Zunfeng Liu [a,b,*]

[a] Key Laboratory of Functional Polymer Materials, College of Chemistry and College of Pharmacy, State Key Laboratory of Medicinal Chemical Biology, Frontiers Science Center for New Organic Matter, Nankai University, Tianjin 300071, China
[b] School of Chemical Engineering, University of Science and Technology Liaoning, Anshan 114051, Liaoning, China
[c] Department of Mechanical Engineering, The University of Texas at Dallas, Richardson, TX 75080, United States
[d] Nanomaterials Physicochemistry Department, Faculty of Chemical Technology and Engineering, West Pomeranian University of Technology, Szczecin, Piastów Ave. 42, 71-065 Szczecin, Poland

## ARTICLE INFO

## ABSTRACT

Increasing mechanical flexibility without sacrificing electrochemical performance of the electrode material is highly desired in the design of flexible electrochemical energy storage devices. In metal-related materials science, decreasing the grain size introduces more grain boundaries; this stops dislocations and crack propagation under deformation, and results in increased strength and toughness. However, such a size refinement effect has not been considered in the mechanical properties, particle stacking, wetting, and electrochemical performances of flexible supercapacitor electrodes. In this paper, MXene was used as an electrode material to study the size refinement effect of flexible supercapacitors. Size refinement improved the strength and toughness of the MXene electrodes, and this resulted in increased flexibility. Finite elemental analysis provided a theoretical understanding of size refinement-increased flexibility. Moreover, the size refinement also improved the specific surface area, electric conductance, ion transportation, and water wetting properties of the electrode, and the size refinement provided highly increased energy density and power density of the MXene supercapacitors. A highly flexible, water-proof supercapacitor was fabricated using size-refined MXene. The current study provides a new viewpoint for designing tough and flexible energy storage electrodes. The size refinement effect may also be applicable for metal ion batteries and electronic and photo devices composed of MXene and other nanoparticles.

© 2021 Science Press and Dalian Institute of Chemical Physics, Chinese Academy of Sciences. Published by ELSEVIER B.V. and Science Press. All rights reserved.

## 1. Introduction

Flexible energy storage devices are in high demand in wearable electronics as flexible power sources that conform to the human body under deformation [1,2]. Improving the flexibility and energy storage performance of the electrodes are highly desired for these electrochemical energy storage devices [3–5]. Flexible supercapacitors are widely studied because of their high-power density, high charge–discharge current density, low cost, and stable cyclability [6,7]. Different strategies have been reported to prepare flexible electrodes for supercapacitors. For example, electrodes can be designed into the shape of fibers [8], thin films [9,10], or foam structures [11] to obtain flexibility. The above strategies increase the bending curvature of flexible electrodes by decreasing the fiber diameter or film thickness or by introducing pores into the electrodes [12–16]. Structural design of flexible electrodes using curved structures like wrinkled [17], buckled [18], folded [19], or coiled structures [20] can further increase the stretchability of electrodes to achieve a large reversible strain. For the above design strategies, supercapacitor electrodes are generally composed of electrochemically active nanoparticles coated on or infiltrated in a flexible substrate or assembled into a free-standing electrode. For example nanocarbon materials (including activated carbon [21], carbon nanotubes (CNTs) [22], graphene [23]), MXene, metal oxides or hydroxides [24,25], or their mixtures have been widely used [26]. During deformation of the above structural designs, the electrode layer was actually subjected to bending deformation,

* Corresponding authors.
    *E-mail addresses:* xchen@zut.edu.pl (X. Chen), bgan@ustl.edu.cn (B. An), liuzunfeng@nankai.edu.cn (Z. Liu).

and the nanoparticles were under tension. The flexibility of the electrode depended on the extent of contact, the interactions of the nanoparticles, and the integrity of the electrode. If there were large cracks in the electrode and the nanoparticles irreversibly separated from each other under deformation, the mechanical properties and the electrochemical activity of the electrodes would be largely deteriorated. Therefore, avoiding large crack generation during electrode deformation while maintaing the electrochemical performances is highly important in the above designs of flexible supercapacitor electrodes.

It is reported that the size of particles in supercapacitor electrodes has a distinct effect on the energy storage performance [27,28]. Decreasing the particle size will increase the specific surface area of the electrode materials, and which facilitates the transfer of electrolyte ions in the electrode and increases the electrochemical performance [29]. However, it is expected that the nanoparticles in a flexible electrode form boundaries between nanoparticles, and this is similar to the case of grains formed by crystals in metals and other materials. For metals, a decrease in the grain size produces more grain boundaries, which stop dislocations and crack growth when the material is under tension. This results in improved mechanical strength and toughness; this is called the "grain refinement effect" and can be expressed as the "Hall-Petch" relationship [30]. The increased toughness and strength enable the material to have larger bending curvature without cracking, which indicates increased flexibility. Although there are reports regarding the effect of particle size on the electrochemical energy storage properties of supercapacitor electrodes, how a particle's size affects electrode flexibility through inhibiting crack generation and propagation has not yet been investigated.

MXene is a type of recently-developed 2D early transition metal carbides, carbonitrides, and nitrides. MXenes show metal-like conductivity, good hydrophilicity, and high mechanical strength. MXenes can be written as the general formula $M_{n+1}X_nT_x$, where M is an early transition metal, X is carbon and/or nitrogen, T is surface functional groups (including –F, –O, and/or –OH), and n is 1, 2, or 3 [31]. $Ti_3C_2T_x$ is the most widely studied of the currently developed different MXenes and it has been investigated as electrochemical electrodes for energy storage devices such as in supercapacitors, metal ion batteries, and in other fields including electromagnetic interference shielding, solar water desalination, catalysis, photoelectricity, and conductive additives [32–34].

$Ti_3C_2T_x$ MXenes have shown high volumetric capacitance when they are assembled into a flexible film. However, the restacking of MXene flakes limits the penetration and transfer of electrolyte ions into the MXene electrode. A general way to inhibit stacking of MXene flakes is to incorporate different species into the MXene flakes; these species include carbon nanotubes, graphene, and polymers (poly dimethyl diallyl ammonium chloride (PDDA), polyvinyl alcohol (PVA), polyaniline (PANI), polypyrrole (PPY), poly(3, 4-ethylenedioxythiophene) (PEDOT)), metal oxides ($RuO_2$ and $Fe_2O_3$), and metal hydroxides (NiOH and Ni-Al hydroxides) [35–40]. The electrochemical performances and flexibility of MXene electrodes are highly improved in this way. However, it has also been discovered that decreasing the thickness of multi-flakes of MXene or decreasing the particle size of MXene results in improved electrochemical performance and mechanical flexibility of MXene electrodes [41,42]. It is expected that the restacking of MXene is highly affected by the size of the flakes; the dependence of electrode properties (such as specific surface area, stacking structure, wetting capabilities, and mechanical flexibility of restacked MXene flakes) on the flake size is worthy of further study. In addition, how the MXene size affects device performance deserves to be studied systematically. The refinement of MXene particle size may have important effects on electrical conductance,

ion transfer, liquid infiltration, particle assembly and aggregation, surface wetting, and mechanical properties.

In this paper, MXene was used as a model particle to investigate the size refinement effect on the mechanical and electrochemical capacitive properties of flexible supercapacitor electrodes (Fig. 1). We firstly developed a fast and scalable method to prepare MXene flakes with well-separated sizes. Briefly, a mechanical and sonication-assisted horizontal filtration (MSHF) method was developed to obtain MXene flakes with well-separated sizes in large quantity using filters with sequentially decreasing hole sizes. MXene flakes were deposited on forest-drawn carbon nanotube sheets (CNTS) to form a CNTS/MXene flexible electrode (Fig. 1e). The size refinement of MXene in the electrode resulted in higher mechanical strength and toughness, and finite elemental modelling (FEM) results agreed well with experimental results. In addition to the mechanical properties, the boundaries between particles in a flexible electrode also affected the transport of ions in the electrolyte. The decrease in MXene size also increased the specific surface area, resulted in loose stacking structure, improved water wetting properties, increased electrical conductivity and ion conductivity, and increased the energy density and power density. The CNTS/MXene electrode showed a curvature of 0.67 mm$^{-1}$ and specific capacitance of 329F g$^{-1}$, and maintained 92% retention after 10,000 charging-discharging cycles. Two series CNTS/MXene electrodes form a water-proof flexible supercapacitor (WFSC). An energy density of 105.9 µWh cm$^{-2}$ was obtained for this flexible supercapacitor at a power density of 0.15 mW cm$^{-2}$. The WFSCs had stable performance at a curvature of 1 cm$^{-1}$ under water and exhibited only ~ 6% fading of the initial capacitance after 1,000 cycles of a folding-twisting test.

## 2. Experimental

### 2.1. Synthesis of MXene

MXene ($Ti_3C_2T_x$) was synthesized from $Ti_3AlT_x$ using the HCl/LiF method [43], which is as follows. First, hydrochloric acid (9 M) was added to a mixture of $Ti_3AlC_2$ (2 g) and LiF (2 g) in a polyethylene beaker and then stirred at 500 rpm for 24 h at 35 °C. The mixture was then rinsed thoroughly via membrane filtration (0.24 µm pore size) until the pH of the solution was > 6. The experiment was carried out in an Ar atmosphere to avoid oxidation of $Ti_3C_2T_x$.

### 2.2. Mechanical and sonication-assisted size grading of MXene

Before size grading experiments, Ar was filled into the vessel for 30 min to remove the oxygen. The as-prepared MXene dispersion in water (2.8 g L$^{-1}$) was then injected into the cylindrical filter with the largest pore size (side length of 21 µm). This was then stirred at a rotational speed of 300 rpm, and the MXene dispersion was passed through the filter and collected. The MXene solution that remained inside the cylindrical filter was collected and used as was. The filtrate was then refiltered using the same filter with a smaller pore size. The above process was repeated until the smallest MXene was collected. The equipment was under sonication only when the filter with the smallest pore size was used. MXene$_x$ samples with five different sizes were obtained using filters with four different pore sizes. The MXene$_x$ samples were freeze-dried for later use.

### 2.3. Preparation of CNTS/MXene$_x$ electrodes and integration of the WFSC device

The CNTS was obtained by drawing a sheet from a carbon nanotube forest on silicon wafers that were grown using the chemical
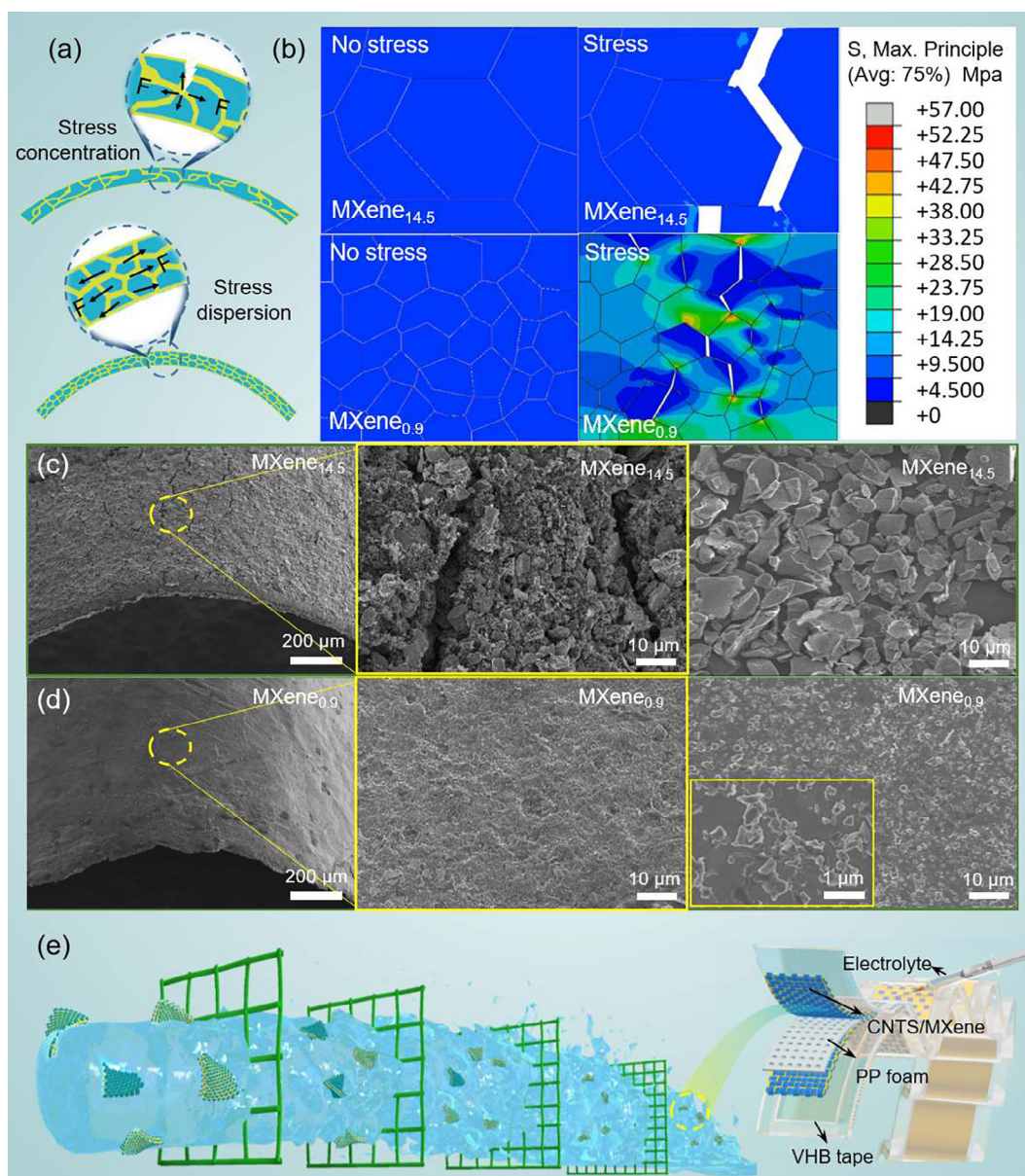
**Fig. 1.** Size-refinement effect on flexible supercapacitor electrodes. (a-d) Schematic diagram (a), FEM results (b), and scanning electron microscopy (SEM) images (c, d) of crack generation in CNTS/MXene$_{14.5}$ and CNTS/MXene$_{0.9}$ electrodes. The two images in the rightmost side of (c) and (d) show pure MXene$_{14.5}$ and MXene$_{0.9}$ flakes, respectively. (e) Schematic diagram of the MSHF method used to obtain MXenes with different sizes and to prepare waterproof flexible supercapacitors.

vapor deposition method; the multi-walled carbon nanotubes had an outer diameter of 9 nm. Two hundred layers of CNTS were stacked to form a thin CNTS film, which was treated with oxygen plasma for 8 s to improve the hydrophilicity. A mixed solution of MXene$_x$ (97 mg) and PVDF (3 mg) in NMP (5 mL) was spray-coated on both sides of the CNTS film to form a flexible CNTS/MXene$_x$ electrode. The electrode was then dried in a vacuum oven at 60 °C for 3 h.

One pair of CNTS/MXene$_{0.9}$ electrodes were attached to both sides of a polypropylene foam (150 μm in thickness) to prepare a single supercapacitor; this was encapsulated using two VHB tapes (Model I49054910) to prepare the WFSC. Six pairs of the CNTS/MXene$_{0.9}$ electrodes were attached to both sides of the polypropylene foam with the neighboring electrodes connected by CNTS to prepare a WFSC made of six-serially connected supercapacitors. The electrolyte contained a mixture of sulfuric acid (1 M) and poly-vinyl alcohol (1 g) in 10 mL of deionized water; a syringe was used

to fill the device with the electrolyte after it mixed in an 85 °C water bath. The size of the VHB tape was a bit larger (10 mm) than the electrodes so that the whole device can be sealed to be water-proof by compressing the edges of the VHB tape.

## 3. Results and discussion

### 3.1. Size grading of MXene using the MSHF method

In this section, we described the detailed size-grading process of MXene using a homemade MSHF setup. MXene was synthesized via the LiF/HCl method with Ti$_3$AlC$_2$, and then it was size graded after it was dispersed in water (2.8 g L$^{-1}$). The separation process was completed with the MSHF system (Fig. 2a). In typical vacuum filtration, the filter membrane or mesh was placed horizontally. Thus, it was easily blocked when particles accumulated on the membrane, and this resulted in decreased filtration speed and poor
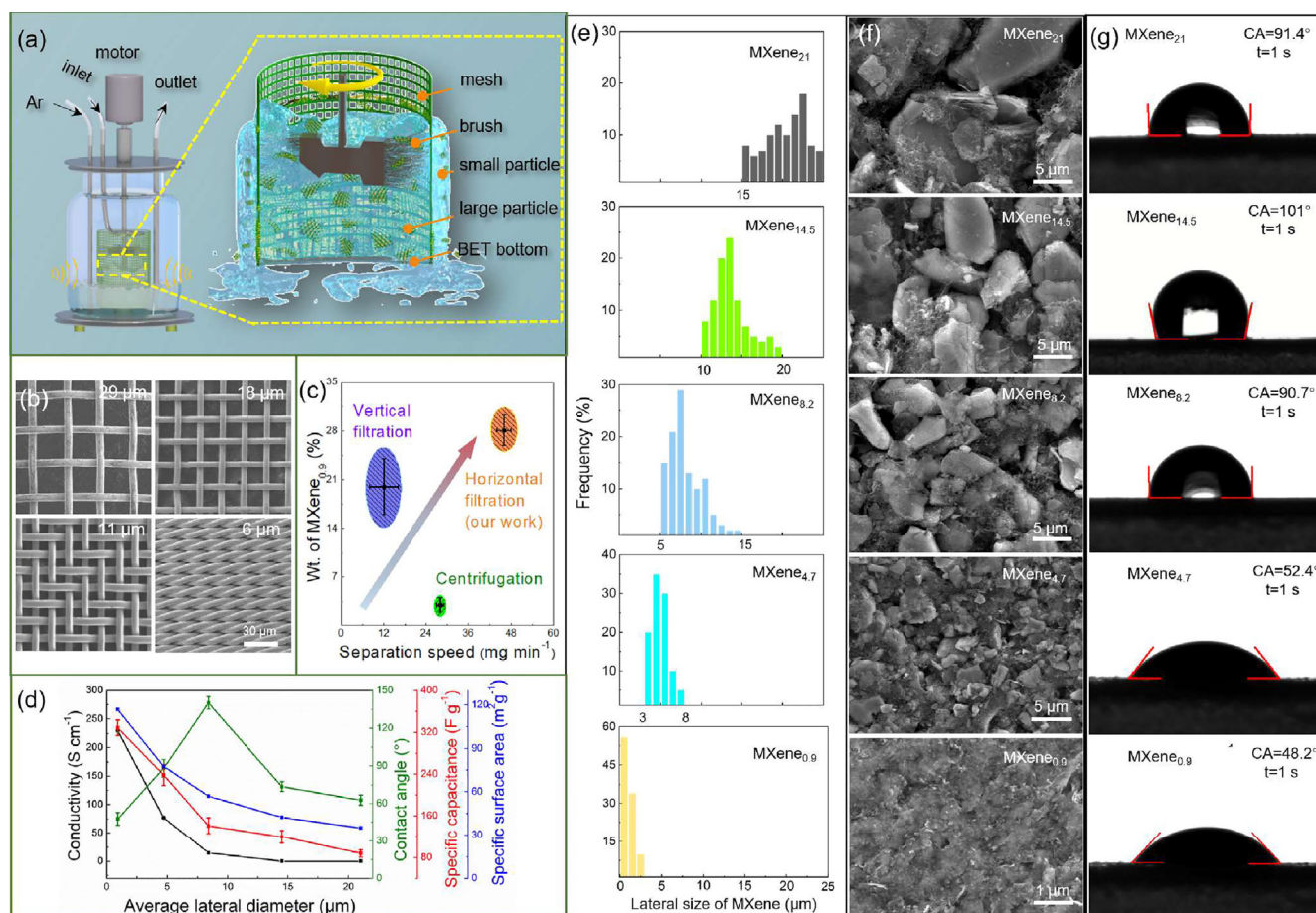
**Fig. 2.** Preparation and properties of MXene flakes with different sizes. (a) Schematic diagram of the equipment used for size grading MXene. (b) SEM images of the stainless steel meshes with different sizes. From left to right, the side length of the pores is 29, 18, 11, and 6 μm (triangle). (c) Comparison of yield and the separation speed for $MXene_{0.9}$ using the MSHF method, centrifugation method, and traditional vertical filtration method (to obtain MXenes with similar average lateral size as that of $MXene_{0.9}$). (d) Size dependence of specific surface area and electrical conductivity for $MXene_x$ membranes prepared via filtration, and water contact angle and specific capacitance for $CNTS/MXene_x$ electrodes. (e) Size distribution of $MXene_x$ with different sizes obtained using the MSHF method. (f) SEM images with high magnifications of the surface of $CNTS/MXene_x$ electrodes. (g) Photographs showing different water contact angles for $CNTS/MXene_x$ electrodes.

separation of MXene particles. To eliminate blockage of the membrane by particle accumulation, a combination of the following four strategies was used. First, instead of using a horizontally-placed film, stainless steel meshes with holes of four different sizes were used; three of these contained square holes with different side lengths (29, 18, 11 μm), and one contained triangle holes with a side length of 6 μm (Fig. 2b). A cylindrical stainless steel mesh was vertically placed on the bottom of a vessel. The water dispersion of MXene was then filled inside this cylindrical filter, and the particles that were smaller than the mesh holes can pass through the mesh. The MXene that remained inside of the cylindrical filter was collected and used as-obtained. The filtrate was then refiltered using a filter with smaller holes to obtain smaller sized MXene. Second, a blender was installed in the center of this cylindrical filter; a blender was used to stir the MXene dispersion and decreased particle accumulation on the mesh holes. Third, there were brushes at the end of the blender, and these scratched the inner surface of the cylindrical filter to remove particles that deposited on the filter. Last, the whole vessel was put inside a bath sonicator, which also helped to remove particles that deposited on the surface of the filter. To avoid MXene oxidation, all of the vessels were filled with Ar. In this way, MXenes with five different sizes were obtained; these were labelled as $MXene_x$, where $x$ represents the average lateral size in microns for the MXene in each sample. Dispersions of $MXene_{21}$, $MXene_{14.5}$, $MXene_{8.2}$, and $MXene_{4.7}$ showed obvious sed-

imentation from hours to days (Fig. S2), but the $MXene_{0.9}$ dispersion was stable for over two weeks without sedimentation.

To quantitatively evaluate this size-grading method, we measured the number frequency of particles for each sample by measuring the lateral size of MXene particles (~200 particles) from five SEM images. As seen, the particle size differed a lot between different samples (Fig. S3a). Even the smallest MXene ($MXene_{0.9}$) showed typical multilayered single crystal sheets, and elemental analysis confirmed the presence of oxygen, carbon, titanium, fluoride, and a tiny amount of aluminum (Fig. S4). For comparison, we conducted a size-grading experiment using centrifugation at different speeds. First, the MXene dispersion was centrifuged at a low speed (e.g., 1,000 rpm), and the sediment that was collected was the large size MXene. The supernatant was then centrifuged at a higher speed (e.g., 3,500 rpm), and the sediment that was collected was the smaller sized MXene. This process was repeated until all of the MXene was collected as sediment. Five centrifugation speeds from 1,000 to 11,000 rpm were used, and five MXene samples were obtained (Fig. S3b). Similarly, the size-distribution of MXene using this centrifugation-based size-grading was also obtained by counting the number frequency of MXene particles. As seen, the size differences for the samples using this centrifugation-based size grading (Fig. S3c) were not as distinct as those prepared using the MSHF method (Fig. 2e).

## 3.2. Characterization of MXene with different sizes and the size-refinement effect on the MXene film properties

Diffraction and spectroscopic properties of MXene$_x$ with different sizes prepared via MSHF were then investigated. The X-Ray diffraction (XRD) patterns of the films that were prepared by stacking of MXene particles showed that the $2\theta$ peak at ~ 7.5° (002 plane) got broader with a decrease in particle size. This indicates less-organized packing between the layers of small-sized MXene, which would facilitate ion transport when it is used for a supercapacitor electrode (Fig. S5). In Fig. S6a, the UV–visible absorption spectroscopy exhibits larger absorption peaks (339 and 887 nm) for MXene$_{0.9}$ than for the other MXene$_x$ samples (314 and 866 nm). It is worth noticing that the five samples had obvious differences in UV absorption in solid UV spectroscopy, and this indirectly reflects a strong UV absorption effect caused by size refinement. We then predicted that size refinement would effectively increase the specific surface area; as expected, the results of the BET test showed that the specific surface area for MXene samples increased from 35.0 to 116.9 m$^2$ g$^{-1}$ with a decrease in the average lateral size from 21 to 0.9 μm (Fig. S6b). Such a large specific surface area is unprecedented for MXene, which generally has a specific surface area below 50 m$^2$ g$^{-1}$ [44–46]. The high specific surface area inevitably facilitates the accessibility of electrolyte ions to MXene particles when it is used for a supercapacitor electrode. In addition, as seen in Fig. S6b, there were mainly mesopores in MXene$_x$, and this is considered to be most conducive to electrolyte wetting and ion transport than micro- and macropores. We then investigated the electrical conductivity of MXene$_x$ film that was prepared from MXenes of different sizes. The MXene$_x$ dispersion in water was vacuum filtered through a membrane (pore size of 0.25 μm) to form a film upon drying. The electrical conductivity was then measured using the four probe method. As seen, the film conductivity increased with a decrease in the size of MXene$_x$ from $1 \times 10^{-4}$ mS cm$^{-1}$ for MXene$_{21}$ to 230 S cm$^{-1}$ for MXene$_{0.9}$ (Fig. 2d). The conductivity of the MXene film increased with a decrease in the particle size. This should be ascribed to the closer packing and increased contact area that result from the size refinement, as seen from the smoother film surface for the smaller MXene particles (Fig. S7a). As a result, the contact resistance between the MXene flakes decreased with a decrease in the particle size, resulting in an increase in the electrical conductivity of the MXene electrode. Interestingly, with an increase in MXene size, the water contact angle for these pure MXene films first increased from 47.6° for MXene$_{0.9}$ to a maximum value of 140.2° for MXene$_{14.5}$, and then decreased to 62.7° for MXene$_{21}$ (Fig. S7b). The poor water wetting on the MXene$_{14.5}$ film should originate from the hierarchical surface that contains micro-nano structures.

## 3.3. Size-refinement effect of MXene on mechanical flexibility

The above characterizations of MXene$_x$ with different sizes prompted us to evaluate their performance when they were used as flexible electrodes in supercapacitors. Such use has been proposed to have important applications in providing an energy supply for wearable electronic devices. Although the MXene film can be obtained via vacuum filtration, it cracked easily under large strain deformation (Fig. S8). Therefore, to avoid cracking of MXene film and to improve charge collection, MXene has generally been coated on nickel foam or carbon cloth when it is used for active material in solid and flexible supercapacitors [47]. However, the thickness of these current collectors was on the millimeter scale, and this resulted in limited flexibility and increased volume of the final devices. To overcome these limitations, we used forest-drawn carbon nanotube sheets as a scaffold to support MXene$_x$,

which served as an electrode in flexible supercapacitors. The CNTS was composed of carbon nanotube (CNT) bundles that had a diameter of about 50 nm (Fig. S9). These CNT bundles showed higher flexibility than materials such as carbon cloth, carbon fiber, and nickel foam. Because the CNT bundles in the CNTS were combined via *van der Waals* forces, the available bending radius of the CNTS was very small (tens of microns). The fabrication procedure was as follows. A mixture of MXene$_x$ and polyvinylidene fluoride (PVDF) adhesive in N-methylpyrrolidone (NMP) was sprayed onto both sides of the CNTS (200 layers, 16 μm in thickness) to form a CNTS/MXene$_x$ composite with a sandwich structure that had a total thickness of 55 μm (Fig. 3a). The composite showed a bending curvature of 0.67 mm$^{-1}$ (left, Fig. 3b) and was wound on a 1.5-mm-diameter rod. The CNTS had a mass density of only 0.7 mg cm$^{-2}$, which was 25 wt% and 26 vol% of the composite electrode. The load mass density of MXene$_{0.9}$ reached 2.8 mg cm$^{-2}$. Furthermore, the mechanical strength and flexibility of the CNTS/MXene$_{0.9}$ composite were much higher than those of the pure MXene$_{0.9}$ film and CNTS (Fig. 3c). Also, the composite can be highly deformed into different shapes without breaking. The breaking strength (40.3 MPa) and breaking strain (21.8%) of the CNTS/MXene$_{0.9}$ composites were respectively 4.9 and 39 times greater than those of the pure MXene$_{0.9}$ film (8.2 MPa and 0.55%). We then tested the mechanical properties of CNTS/MXene$_x$ composites containing MXenes with different sizes (Fig. 3d). It was observed that the tensile strength of the CNTS/MXene$_x$ composite decreased with an increase in the flake size of the MXenes. The CNTS/MXene$_{0.9}$ composite showed the highest breaking strength (43 MPa) and fracture strain (23%) compared to the other samples. This indicates that the size-refinement effect of MXenes improve the mechanical properties of CNTS/MXene$_x$ electrodes. Microscopy and contact angle measurements of the CNTS/MXene$_x$ composites (Fig. 2f, 2g, and S10) indicate similar trends for the morphological and wetting properties as those of the pure MXene$_x$ films with a decreasing MXene flake size.

## 3.4. Theoretical modeling of size-refinement effects on the mechanical properties of CNTS/MXene electrodes

In this section, we provide results from theoretical modeling of the effects that size refinement has on the mechanical properties of CNTS/MXene electrodes. Simulations based on FEM were performed to elucidate the mechanism of the experimentally observed tensile failure of the CNTS/MXene$_x$ composites. First, the model constructed using the CNTS/MXene$_{0.9}$ composite as an example is described. Because the experimental CNTS/MXene$_{0.9}$ electrode sample had a three-layer structure, a computer aided engineering (CAE) model was first created as a sandwich structure, where the center layer was CNTS and the two outer layers were MXene/PVDF films. The dimensions of this CAE structure are shown in Fig. S11, and the thickness was the same as that of the experimental samples. Because the width (0.5 cm) of this sample was much larger than its thickness (55 μm), the problem was considered to be a plane stress problem. The whole simulation was considered in two steps. First, we used a homogeneous model to acquire the macromechanical properties of the CNTS/MXene$_x$ composite and the macromaterial properties of the corresponding CNTS and MXene. Then, we used the calibrated macromaterial properties to create the microstructure of the CNTS/MXene$_x$ composite containing MXenes with different flake sizes to further elucidate the mechanism. The simulation model was constructed with the structure shown in Fig. S11 using the mechanical properties of CNTS (Fig. 3c) and the calibrated MXene/PVDF layer (Fig. S12). Fig. 3c shows the stress–strain curve of the CNTS/MXene$_{0.9}$ composite in the CAE model, and this agrees well with the experimental results.
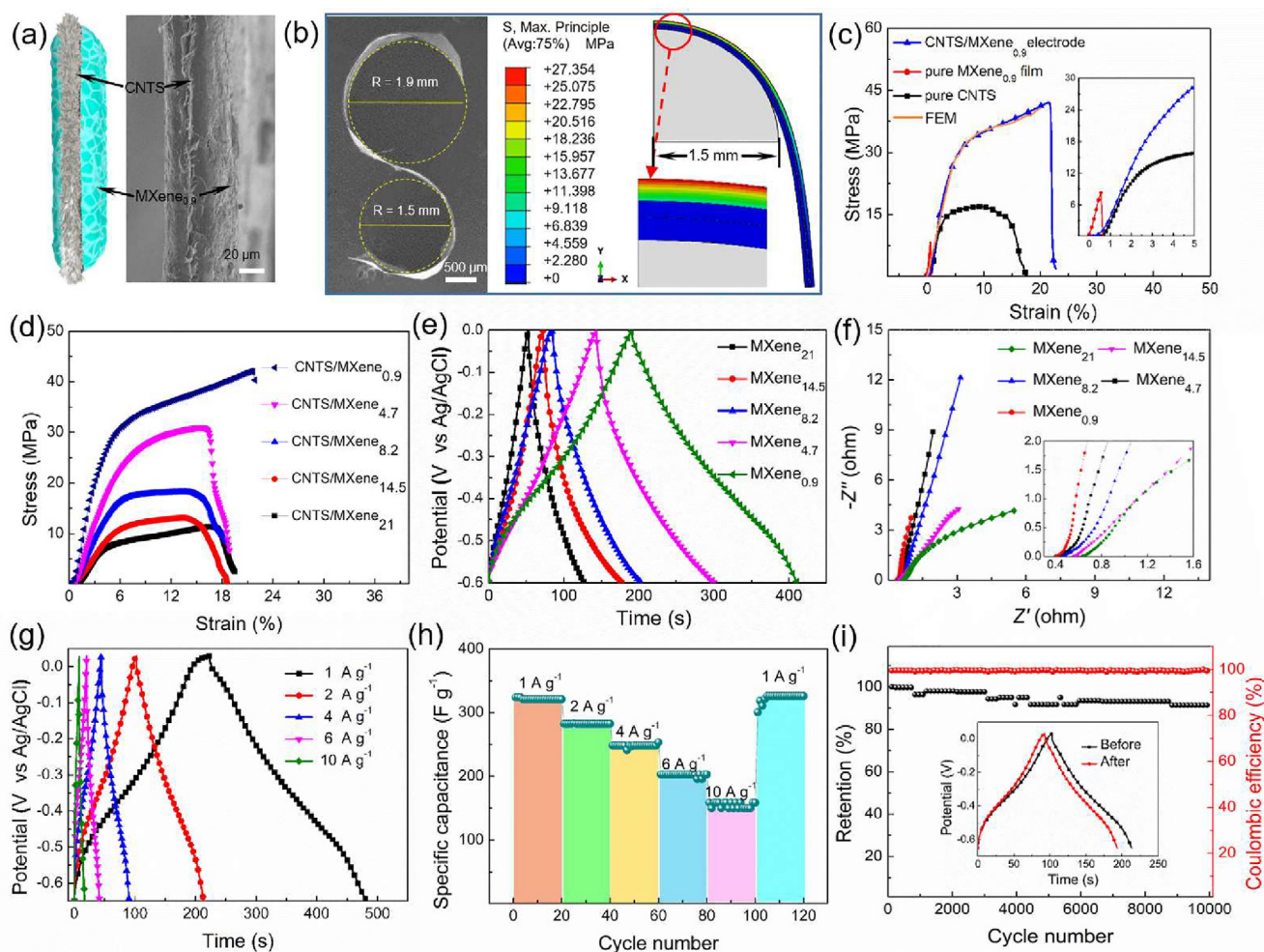
**Fig. 3.** Size-refinement effect on the supercapacitor performance. (a) Schematic diagram of the structure and SEM images of the CNTS/MXene$_{0.9}$ electrode. (b) SEM image (left) and the results of the bending simulation (right) of the MXene$_{0.9}$ electrode at a curvature of 0.67 mm$^{-1}$. (c) Stress–strain curves of the CNTS/MXene$_{0.9}$ electrode film, MXene$_{0.9}$ film, CNTS, and the FEM results. (d) Stress–strain curves, (e) GCD curves at 1 A g$^{-1}$ current density, and (f) Nyquist plots for the CNTS/MXene$_x$ electrodes. The inset of (f) shows a magnified view of the region at high frequency. (g) GCD curves at different current densities, (h) specific capacitance for 20 charge/discharge cycles at different current densities, and (i) retention of specific capacitance and coulombic efficiency under 10,000 cycles for the CNTS/MXene$_{0.9}$ electrode; the inset shows GCD curves before and after 10,000 charge/discharge cycles.

The left image in Fig. 3b shows that CNTS/MXene$_{0.9}$ can be wrapped around large-curvature rods without damage (with rod diameters of 1.9 and 1.5 mm), indicating high flexibility. The right image in Fig. 3b shows results of the bending simulation of the CNTS/MXene$_{0.9}$ composite in the CAE model. The sandwich structure of CNTS/MXene$_{0.9}$ was assigned as the calibrated material; the tensile strength in the bending simulation was very close to the experimental results. The theoretically simulated CNTS/MXene$_{0.9}$ film was not damaged after it was wrapped on a 1.5 mm diameter cylinder, and the value of the maximum principal stress (27 MPa) in the membrane structure was less than the breaking strength (40 MPa).

On the basis of the above FEM model for CNTS/MXene$_x$, we simulated the crack growth process of CNTS/MXene$_x$ electrodes containing MXene particles with significantly different particle sizes (MXene$_{0.9}$ and MXene$_{14.5}$) under stress conditions (Fig. 1a, 1b and movie S1). The left images of Fig. 1b show the CAE model of the above two CNTS/MXene electrodes without stress. The MXene$_{0.9}$ electrode contained more fixed boundaries between MXene flakes than the MXene$_{14.5}$ electrode. Under stress (right images in Fig. 1b), the unbound boundaries caused high stress concentration, and crack propagation occurred. The two images on the right of Fig. 1b show the results of comparing CNTS/MXene$_{0.9}$ and

CNTS/MXene$_{14.5}$, and this comparison indicates that the maximum principal stress was at the same elongation (4%). After the first crack, the stress concentration of the MXene$_{14.5}$ model was higher than that of the MXene$_{0.9}$ model. This indicates the reason why the MXene$_{14.5}$ model quickly totally fails; specifically, the MXene$_{0.9}$ model could still transfer stress from the inner connection structure, inhibiting crack propagation.

Then, we carried out bending experiments on the CNTS/MXene$_{14.5}$ and CNTS/MXene$_{0.9}$ electrodes and the surface morphologies were shown in SEM. Fig. 1c and 1d show the surface morphologies of the two electrodes after they were bent to a curvature of 0.67 cm$^{-1}$. Large cracks were observed in the CNTS/MXene$_{14.5}$ electrode, whereas there were no visible cracks in the CNTS/MXene$_{0.9}$ electrode indicating the effect that the size refinement of the MXene flakes has on the MXene electrode.

### 3.5. Size-refinement effect on capacitive performance of CNTS/MXene electrodes

The electrochemical properties of the CNTS/MXene$_x$ electrodes was investigated in a three-electrode system. Cyclic voltammetry (CV) curves at scanning rate of 10 mV s$^{-1}$ (Fig. S13a) and galvanostatic charge–discharge (GCD) curves at 1 A g$^{-1}$ are shown in

Fig. 3e, which shows that the specific capacitance increased with a decrease in the size of MXene; the specific capacitance was 88.4, 120.1, 141.2, 238.7, and 318.5F g$^{-1}$ for MXene$_{21}$, MXene$_{14.5}$, MXene$_{8.2}$, MXene$_{4.7}$, and MXene$_{0.9}$, respectively, over a potential range of −0.6 to 0 V. The redox peak should be ascribed to the CNTs present in the electrode and generally observed for the CNT based electrode [20,48]. The Nyquist plots in electrochemical impedance spectroscopy (EIS) from 100 kHz to 10 MHz for the CNTS/MXene$_x$ electrodes were used to further evaluate the ion and charge transport in the electrodes (Fig. 3f). Compared to the other MXene samples, MXene$_{0.9}$ had the smallest semicircle in the high frequency region and the highest slope for the straight line in the low frequency region. These observations indicate that MXene$_{0.9}$ had the smallest interfacial charge transfer resistance and the highest ion diffusion. This agrees with the fact that MXene$_{0.9}$ presented the highest electrical conductivity, smallest water contact angle, and largest specific surface area. CNTS/MXene$_{0.9}$ was then measured using CV curves at different scanning rates (Fig. S13b) and GCD curves at different current densities (Fig. 3g). The highest specific capacitance (329 F g$^{-1}$) was obtained at a current density of 1 A g$^{-1}$ over a potential range from −0.65 to + 0.03 V; this is one of the best results for MXene-based electrodes in literatures (Table S1). Even so, without considering the preparation of a flexible electrode, it is possible to further improve the potential range by optimizing the three electrode system using glassy carbon (or graphite or titanium) as the current collector and activated carbon electrode as counter electrode in future work [49,50].

To further investigate the size-refinement effect in terms of the pseudocapacitance contribution, we calculated the capacitive contribution of the MXene electrodes with different MXene sizes (Fig. S14). With a decrease in MXene size, the relative capacitive contribution increased. In addition, the absolute values of both diffusion and capacitive induced capacitance increased with a decrease in MXene size. This agrees with the fact that with a decrease in MXene size, we observed increased specific surface area (from BET results), increased film electrical conductivity (from conductivity results), nonuniform packing of MXene flakes (from XRD results), and SEM observations. X-ray photoelectron spectroscopy (XPS) analysis was carried out to compare the surface terminations of MXene with different size, as shown in Fig. S15. We found the survey spectra of the corresponding samples exhibited an obvious increase in the element oxygen and a decrease in element fluoride (Figs. S15a and b). Specifically, as shown in Fig. 15c, the oxygen content in MXene$_{0.9}$ was estimated to be 28%, whereas the oxygen contents in MXene$_{21}$ was only 13%. Meanwhile, the fluoride content for MXene$_{0.9}$ (0.9%) was much smaller than that of MXene$_{21}$ (21%). It is clear that bonding between oxygen functional groups and the hydronium ion from H$_2$SO$_4$ electrolyte occurs during the charging process, and the change of Ti oxidation state leads to high pseudocapacitance [51]. However, the fluoride terminations of MXene are detriment to charge storage, and −F is not known to participate in any pseudocapacitive energy storage processes [52]. According to this mechanism, the increased amount of the − O terminal groups, or the decreased amount of the − F terminal groups may result in the highly improved electrochemical supercapacitance. There may other two reasons for the high specific capacitance. First, the highly aligned CNTS provides channels for the penetration of protons and shows enhanced wettability in the electrolyte after the oxygen plasma treatment. This ensures good contact between the CNTS and the PVA electrolyte as well as rapid charge transfer along the aligned direction of CNTS. Second, because there is a large number of mesoporous structures in densely packed MXene$_{0.9}$, its unprecedented effective reaction area allowed ion transport and provided enough space for volume change during doping and undoping pseudocapacitance processes. The specific capaci-

tance at 1 A g$^{-1}$ showed a negligible decrease after GCD cycling at consecutively increased current density (Fig. 3h). Also, there was 92% retention of the specific capacitance, and 100% of the column efficiency was retained after 10,000 cycles at 2 A g$^{-1}$ current density (Fig. 3i) with the charge–discharge profile slightly changed (the inset of Fig. 3i). Among all of the investigated samples, the CNTS/MXene$_{0.9}$ electrodes showed the most stable electrochemical performance (Fig. S15a). This is a result of the uniform packing and assembly of the MXene particles in the MXene film and the steric shielding effect of acid along the edges [53]. In addition, after 10,000 charge/discharge cycles, XRD results show that there was negligible oxidation of the CNTS/MXene$_{0.9}$ film (Fig. S15b), and this proves the good stability of the film.

SEM pictures of the CNTS/MXene$_{0.9}$ electrode after 10,000 charge/discharge cycles (Fig. S10f) show that after a long period of cycling, no cracks were observed on the surface of the CNTS/MXene$_{0.9}$ electrode with slight buckling. This indicates that the MXene electrode remained intact during insertion/de-insertion of ions during the charge/discharge process. This good cycling capacity of the MXene electrode was also observed in other types of devices (e.g., zinc ion batteries), where high cycling stability, good electrochemical performance, and high capacity retention were achieved [54,55].

The rate performance of electrodes with different particle sizes were also compared together (Fig. S16). The capacitance retention increased with a decrease in the particle size and with an increase in the current density from 1 to 5 A g$^{-1}$. The capacitance retention was 74% and 43% for the CNTS/MXene$_{0.9}$ and CNTS/MXene$_{21}$, respectively, with an increase in the current density from 1 to 5 A g$^{-1}$.

Among the MXene samples in this work, the MXene with the smallest size (MXene$_{0.9}$) showed the best supercapacitive performance; thus, we then calculated the yield of MXene$_{0.9}$ (28.1 wt%) and other MXene$_x$ samples using the proposed MSHF method (Fig. S17a). For comparison, vertical filtration using mesh with the same size used to produce MXene$_{0.9}$ was used to collect the small size MXene; the produced yield was 19% because of filter blocking. Alternatively, centrifugation between 8500 rpm and 11000 rpm also produced MXene that had a similar average size as MXene$_{0.9}$, but the yield was only 3% (Fig. S17b). Moreover, the speed used to obtain MXene$_{0.9}$ with the MSHF method was much faster than for the vacuum filtration using a horizontally placed membrane and centrifugation. The MSHF method provided high MXene separation efficiency because the MXene separation speed did not get slow during long-time filtration, and the equipment can remain oxygen-free during filtration. In the current work, a medium-scale grading device was prepared to demonstrate the possibility of size grading of MXene. For large-scale production, there are three considerations to improve the efficiency. First, the volume of the filter drum can be increased to allow a larger amount of MXene solution to be treated; at the same time, increasing the pump power and pipe diameter help improve the filtration speed. Second, several filter drums with different sizes can be put in the size-grading device to allow serial filtration and size grading. Third, alternatively, several MSHF devices containing filters with different pore sizes can be connected in series to allow continuous production of MXenes with different sizes.

### 3.6. Water proof flexible supercapacitors using CNTS/MXene$_{0.9}$ electrodes

To evaluate the feasibility of using size-graded MXene$_{0.9}$ as water-proof flexible supercapacitors, A symmetrical supercapacitor was assembled by attaching two CNTS/MXene$_{0.9}$ electrodes to both sides of a polypropylene foam; a mixture of sulfuric acid (1 M, 10 ml) and polyvinyl alcohol (1 g) was used as the electrolyte,

and the device was sealed using two pieces of VHB adhesive tape (Fig. 4a). Six supercapacitors were connected in series to form a WFSC device. In this device, metal components were not used as the current collector or connectors to neighboring supercapacitors. Therefore, this device avoids the hidden danger of an open circuit and contact resistance caused by the grafted metal current collector during bending and twisting deformation; thus, the WFSC can withstand higher mechanical forces. The device was very flexible (movie S2) and can be highly twisted, folded, and wound around a finger. Because of VHB's hydrophobic surface and superior adhesion, there was no leakage even when a large amount of electrolyte was added, and this device was highly stable under water (Fig. 4b). The current-constant charge–discharge curves were recorded at different current densities over the potential range of 0 to 0.8 V

(Fig. 4c). The maximum areal specific capacitance (281 mF cm$^{-2}$) was obtained at a current density of 1.5 mA cm$^{-2}$. The GCD curves showed good retention after 500 twisting/untwisting cycles (96.6%) and then after 500 bending/unbending cycles (93.7%); the device was then kept in an atmosphere of air for two weeks (91.0%) and then stored under water for 48 h (90.7%) (Fig. 4d). Such good retention is critical for practical use in flexible energy storage devices. Performance retention after deformation showed that the combination of MXene and CNTS was very strong, and we assume that this results from the porous structure of the CNTS aerogel; this allowed the MXene flakes to become embedded between the CNT bundles during spray coating of the MXene slurry, and the CNT bundles formed strong interactions with MXene after the solvent evaporated.
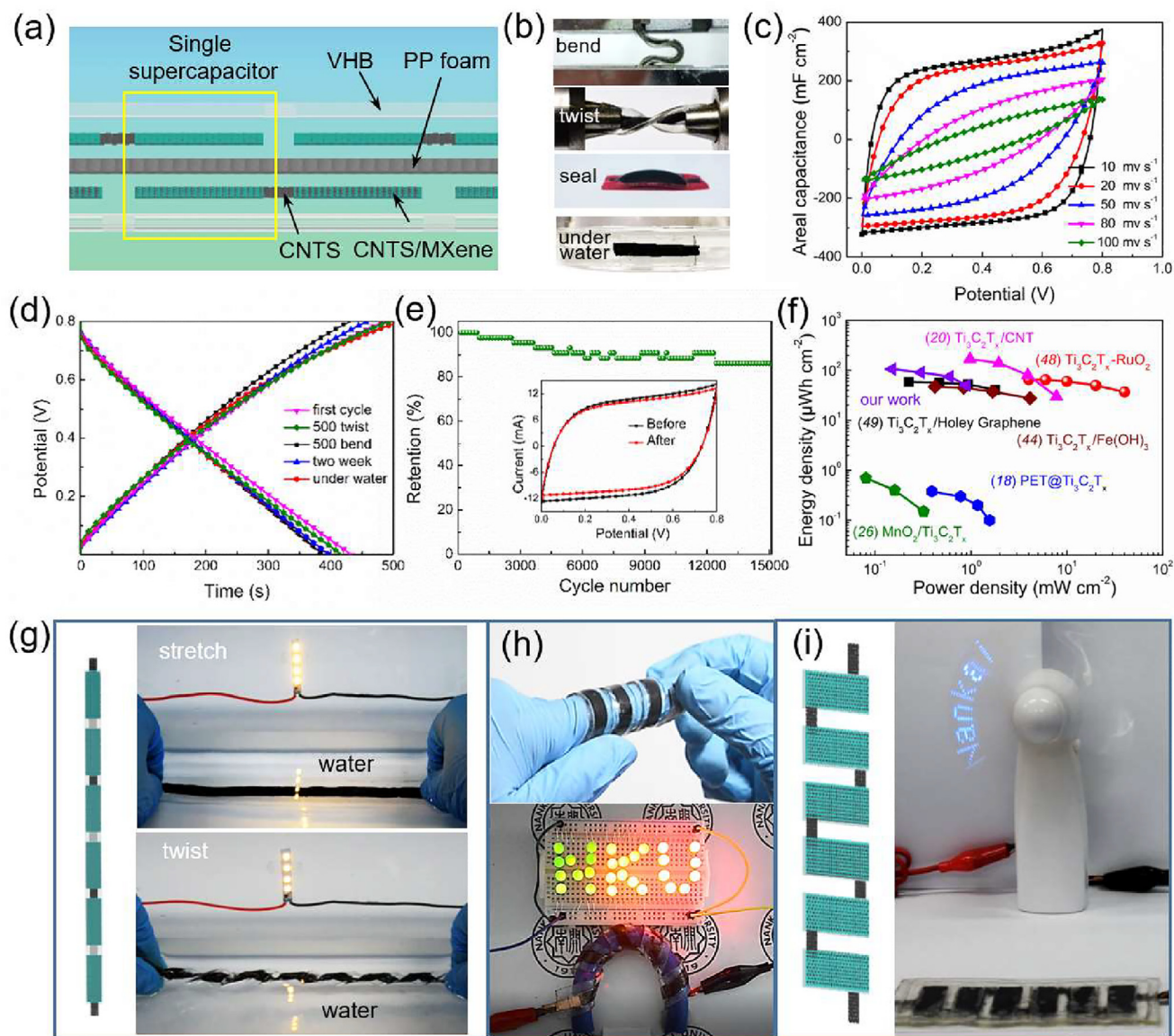


**Fig. 4.** Performance of the WFSC with size-refined electrodes. (a) Schematic diagram of the device design and (b) photographs of a WFSC. (c) CV curves of a single WFSC at different scan rates. (d) GCD curves of a WFSC before and after 500 cycles of bending, after 500 cycles of twisting, after storage for two weeks, and then after storage in water for 48 h. (e) Retention of specific capacitance for 15,000 charge/discharge cycles at 15 mA cm$^{-2}$; the inset shows CV curves at 10 mV s$^{-1}$ before and after 15,000 charge/discharge cycles. (f) Ragone plots showing the energy density as a function of power density for the supercapacitor in this work compared to literature results. (g) Photographs showing an LED light powered by a WFSC prepared using six flexible supercapacitors connected in series before and after twisting under water. (h) (Top) WFSC wrapped around an index finger; (bottom) photograph showing an LED panel demonstrating characters of "NKU" powered by a WFSC prepared using flexible supercapacitors connected in series and wound around a 1-cm-diameter mandrel. Each supercapacitor in (g) and (h) had a length of 2 cm and a width of 0.5 cm. (i) Electric fan (4 V, 5 W) powered by a WFSC prepared using six flexible supercapacitors connected in series. Each supercapacitor in (i) was 3 cm long and 1 cm wide.

About 88.9% of the specific capacitance was retained after 15,000 charge/discharge cycles, and there was negligible change in the CV curves during this cycling test (Fig. 4e). We observed that there are some slight fluctuations in the curves shown in Fig. 3i, 3H, and 4e, which was also reported in the literature [56,57]. The reason for this might be as follows: in the electrochemical reaction process, the activation of the electrode, which is caused by the enhanced electrolyte transportation and proton intercalation, contributes to an increase in capacitance; in contrast, the expansion and collapse of the microstructure of the electrode, which is caused by proton intercalation, lead to a decrease in capacitance. The combination of these two effects results in a slight disturbance in capacity measurements. Fig. 4f shows a comparison of the Ragone plots of the flexible CNTS/MXene$_{0.9}$ supercapacitor with typical flexible supercapacitors made of other MXene electrodes, as reported in the literature. Our flexible supercapacitor shows energy densities of 105.9 and 50 μWh cm$^{-2}$ at power densities of 0.15 and 0.9 mW cm$^{-2}$, respectively. Although MXene$_x$ was not mixed with other metal oxides before it was coated on CNTS, the performance of the resulting flexible supercapacitor was among the best of the MXene-composite-based flexible supercapacitors, including Ti$_3$C$_2$T$_x$/holy graphene (12.1 μWh cm$^{-2}$ for 40 mW cm$^{-2}$) [58], Ti$_3$C$_2$T$_x$/carbon nanotubes (7.8 μWh cm$^{-2}$ for 30 mW cm$^{-2}$) [20], and Ti$_3$C$_2$T$_x$/RuO$_2$ (37 μWh cm$^{-2}$ for 40 mW cm$^{-2}$) [47]. Six serially connected supercapacitors (2 cm in length and 0.5 cm in width, for each supercapacitor) were used as the electric power supply to light an 800 mW light emitting diode (LED) for over eight minutes (Fig. 4g) and even to drive a small fan (Fig. S18). High twisting, bending, or immersing in a water bath did not affect the lighting of the LED light (Fig. 4g, movie S2). The ability of WFSC to be wrapped around a finger indicates its high flexibility (top of Fig. 4h). Moreover, winding the WFSC device around a 1-cm-diameter mandrel can provide a stable power supply for 29 LEDs (bottom of Fig. 4h). The curvature of the WFSC device was calculated to be 1 cm$^{-1}$. Larger sized supercapacitors (3 cm in length and 1 cm in width, for each supercapacitor) were connected in series to run an electric fan (Fig. 4i; movie S3). The above results indicate that the MXene$_x$ obtained via MSHF can be used as an effective electrode material for waterproof flexible supercapacitors, and the design of a WFSC device provided ideas for highly practical flexible energy storage devices.

## 4. Conclusions

Grain refinement has been widely studied for metal and materials science, specifically in terms of how it enhances mechanical strength and toughness. However, this effect has not been considered in the electrode materials of flexible supercapacitors with respect to the mechanical and capacitive performance. In this paper, the size-refinement effect is similar to the grain-refinement effect and was investigated for a flexible supercapacitor electrode using MXene as the electrode material. MXene with different sizes was obtained using a vertically placed filter assisted by stirring and sonication. The flexible electrode was prepared by coating MXene on forest drawn carbon nanotube sheets. Finite elemental analysis provided a theoretical understanding of the size-refinement effect on increased flexibility. The size-refinement of MXene improved the mechanical strength and toughness of the flexible electrode. This also resulted in increased specific surface area, electrical conductance, enhanced ion transportation, and improved water wetting properties of the electrode. The MXene electrode showed a specific capacitance of 329F g$^{-1}$ under 0.68 V potential. A flexible, waterproof supercapacitor was fabricated. The supercapacitor showed an energy density of 105.9 μWh cm$^{-2}$ at a power density of 0.15 mW cm$^{-2}$ and 88.9% retention

of the specific capacitance after 15,000 charge/discharge cycles. The current study suggests an important aspect of size refinement that should be considered in designing a flexible energy storage field. Size-refinement had important effects on particle assembly, surface properties, and mechanical properties and may also be applicable in metal ion batteries and electronic and photo devices composed of MXene and other nanoparticles.

## Declaration of Competing Interest

The authors declare that they have no known competing financial interests or personal relationships that could have appeared to influence the work reported in this paper.

## Appendix A. Supplementary data

Supplementary data to this article can be found online at https://doi.org/10.1016/j.jechem.2021.08.034.

## References

[1] Y. Zhou, X. Wang, L. Acauan, E. Kalfon-Cohen, X. Ni, Y. Stein, K.K. Gleason, B.L. Wardle, Adv. Mater. 31 (2019) 1901916.
[2] K. Keum, J.W. Kim, S.Y. Hong, J.G. Son, S.S. Lee, J.S. Ha, Adv. Mater. (2020) 2002180.
[3] H. Li, Z. Tang, Z. Liu, C. Zhi, Joule 3 (2019) 613–619.
[4] C. Xiang, Z. Wang, C. Yang, X. Yao, Y. Wang, Z. Suo, Mater. Today 34 (2020) 7–16.
[5] K. Youssef, Y. Li, S. O'Keeffe, L. Li, Q. Pei, Adv. Funct. Mater. 30 (2020) 1909102.
[6] Z. Ren, J. Yu, Y. Li, C. Zhi, Adv. Energy Mater. 8 (2018) 1702467.
[7] Y. Guo, K. Zheng, P. Wan, Small 14 (2018) 1704497.
[8] C. Yu, Y. Gong, R. Chen, M. Zhang, J. Zhou, J. An, F. Lv, S. Guo, G. Sun, Small 14 (2018) 1801203.
[9] J. Meng, F. Zhang, L. Zhang, L. Liu, J. Chen, B. Yang, X. Yan, J. Energy Chem. 46 (2020) 256–263.
[10] X. Wang, L. Dong, W. Liu, Y. Huang, X. Pu, J. Wang, F. Kang, J. Li, C. Xu, J. Energy Chem. 48 (2020) 233–240.
[11] T.H. Chang, T. Zhang, H. Yang, K. Li, Y. Tian, J.Y. Lee, P.Y. Chen, ACS Nano 12 (2018) 8048–8059.
[12] S.-H. Park, P.J. King, R. Tian, C.S. Boland, J. Coelho, C. Zhang, P. McBean, N. McEvoy, M.P. Kremer, D. Daly, J.N. Coleman, V. Nicolosi, Nat. Energy 4 (2019) 560–567.
[13] X. Zhang, Z. Lin, B. Chen, S. Sharma, C.-P. Wong, W. Zhang, Y. Deng, J. Mater. Chem. A 1 (2013) 5835.
[14] Z. Weng, Y. Su, D.-W. Wang, F. Li, J. Du, H.-M. Cheng, Adv. Energy Mater. 1 (2011) 917–922.
[15] M. Guo, C. Liu, Z. Zhang, J. Zhou, Y. Tang, S. Luo, Adv. Funct. Mater. 28 (2018) 1803196.
[16] J. Come, J.M. Black, M.R. Lukatskaya, M. Naguib, M. Beidaghi, A.J. Rondinone, S.V. Kalinin, D.J. Wesolowski, Y. Gogotsi, N. Balke, Nano Energy 17 (2015) 27–35.
[17] Z. Zhou, W. Panatdasirisuk, T.S. Mathis, B. Anasori, C. Lu, X. Zhang, Z. Liao, Y. Gogotsi, S. Yang, Nanoscale 10 (2018) 6005–6013.
[18] W. Shao, M. Tebyetekerwa, I. Marriam, W. Li, Y. Wu, S. Peng, S. Ramakrishna, Y. Yang, M. Zhu, J. Power Sources 396 (2018) 683–690.
[19] S. Jiao, A. Zhou, M. Wu, H. Hu, Adv. Sci. 6 (2019) 1900529.
[20] Z. Wang, S. Qin, S. Seyedin, J. Zhang, J. Wang, A. Levitt, N. Li, C. Haines, R. Ovalle-Robles, W. Lei, Y. Gogotsi, R.H. Baughman, J.M. Razal, Small 14 (2018) 1802225.

[21] T. Lv, M. Liu, D. Zhu, L. Gan, T. Chen, Adv. Mater. 30 (2018) e1705489.
[22] L. Yang, W. Zheng, P. Zhang, J. Chen, W.B. Tian, Y.M. Zhang, Z.M. Sun, J. Electroanal. Chem. 830 (2018) 1–6.
[23] J. Miao, Q. Zhu, K. Li, P. Zhang, Q. Zhao, B. Xu, J. Energy Chem. 52 (2021) 243–250.
[24] H. Li, Y. Gao, C. Wang, G. Yang, Adv. Energy Mater. 5 (2015) 1401767.
[25] J. Hanmei, W. Zegao, Y. Qian, H. Muhammad, W. Zhiming, D. Lichun, D. Mingdong, Electrochim. Acta 290 (2018) 695–703.
[26] Y. Jiang, C. Zhou, J. Liu, Energy Storage Mater. 11 (2018) 75–82.
[27] G.G. Jang, B. Song, K.-S. Moon, C.-P. Wong, J.K. Keum, M.Z. Hu, Carbon 119 (2017) 296–304.
[28] L. Alexey, L. Haidong, A. Mohamed, A. Babak, G. Alexei, G. Yury, S. Alexander, Sci. Adv. 4 (2018) eaat0491.
[29] M. Lu, W. Han, H. Li, W. Zhang, B. Zhang, J. Energy Chem. 48 (2020) 344–363.
[30] H. Ryou, J.W. Drazin, K.J. Wahl, S.B. Qadri, E.P. Gorzkowski, B.N. Feigelson, J.A. Wollmershauser, ACS Nano 12 (2018) 3083–3094.
[31] J. Zhou, J. Yu, L. Shi, Z. Wang, H. Liu, B. Yang, C. Li, C. Zhu, J. Xu, Small 14 (2018) 1803786.
[32] H. Zhang, L. Wang, C. Shen, G. Qin, Q. Hu, A. Zhou, Electrochim. Acta 248 (2017) 178–187.
[33] A. VahidMohammadi, M. Mojtabavi, N.M. Caffrey, M. Wanunu, M. Beidaghi, Adv. Mater. 31 (2019) 1806931.
[34] L. Qin, Q. Tao, A. El Ghazaly, J. Fernandez-Rodriguez, P.O.Å. Persson, J. Rosen, F. Zhang, Adv. Funct. Mater. 28 (2018) 1703808.
[35] N. Michael, K. Murat, P. Volker, L. Jun, N. Junjie, H. Min, H. Lars, G. Yury, M.W. Barsoum, Adv. Mater. 23 (2011) 4248–4253.
[36] Z. Ling, C.E. Ren, M.Q. Zhao, J. Yang, J.M. Giammarco, J. Qiu, M.W. Barsoum, Y. Gogotsi, Proc. Natl. Acad. Sci. 111 (2014) 16676–16681.
[37] S. Tu, Q. Jiang, X. Zhang, H.N. Alshareef, ACS Nano 12 (2018) 3369–3377.
[38] M. Boota, Y. Gogotsi, Adv. Energy Mater. 9 (2019) 1802917.
[39] H. An, T. Habib, S. Shah, H. Gao, M. Radovic, M.J. Green, J.L. Lutkenhaus, Sci. Adv. 4 (2018) eaaq0118.
[40] J. Zhang, N. Kong, S. Uzun, A. Levitt, S. Seyedin, P.A. Lynch, S. Qin, M. Han, W. Yang, J. Liu, X. Wang, Y. Gogotsi, J.M. Razal, Adv. Mater. 32 (2020) e2001093.
[41] X. Li, Y. Ma, P. Shen, C. Zhang, X. Yan, Y. Xia, S. Luo, Y. Gao, ChemElectroChem 7 (2020) 821–829.
[42] K. Maleski, C.E. Ren, M.Q. Zhao, B. Anasori, Y. Gogotsi, A.C.S. Appl, Mater. Inter. 10 (2018) 24491–24498.
[43] M. Alhabeb, K. Maleski, B. Anasori, P. Lelyukh, L. Clark, S. Sin, Y. Gogotsi, Chem. Mater. 29 (2017) 7633–7644.
[44] Z. Fan, Y. Wang, Z. Xie, X. Xu, Y. Yuan, Z. Cheng, Y. Liu, Nanoscale 10 (2018) 9642–9652.
[45] H. Li, X. Li, J. Liang, Y. Chen, Adv. Energy Mater. 9 (2019) 1803987.
[46] J. Li, X. Yuan, C. Lin, Y. Yang, L. Xu, X. Du, J. Xie, J. Lin, J. Sun, Adv. Energy Mater. 7 (2017) 1602725.
[47] Q. Jiang, N. Kurra, M. Alhabeb, Y. Gogotsi, H.N. Alshareef, Adv. Energy Mater. 8 (2018) 1703043.
[48] M.Q. Zhao, C.E. Ren, Z. Ling, M.R. Lukatskaya, C. Zhang, K.L. Van Aken, M.W. Barsoum, Y. Gogotsi, Adv. Mater. 27 (2015) 339–345.
[49] M.R. Lukatskaya, S. Kota, Z.F. Lin, M.Q. Zhao, N. Shpigel, M.D. Levi, J. Halim, P.L. Taberna, M. Barsoum, P. Simon, Y. Gogotsi, Nat. Energy 2 (2017) 17105.
[50] W. Tian, A. VahidMohammadi, M.S. Reid, Z. Wang, L. Ouyang, J. Erlandsson, T. Pettersson, L. Wagberg, M. Beidaghi, M.M. Hamedi, Adv. Mater. 31 (2019) e1902977.
[51] H. Shao, K. Xu, Y.-C. Wu, A. Iadecola, L. Liu, H. Ma, L. Qu, E. Raymundo-Piñero, J. Zhu, Z. Lin, P.-L. Taberna, P. Simon, ACS Energy Lett. 5 (2020) 2873–2880.
[52] X. Chen, Y. Zhu, M. Zhang, J. Sui, W. Peng, Y. Li, G. Zhang, F. Zhang, X. Fan, ACS Nano 13 (2019) 9449–9456.
[53] X. Zhao, A. Vashisth, J.W. Blivin, Z. Tan, D.E. Holta, V. Kotasthane, S.A. Shah, T. Habib, S. Liu, J.L. Lutkenhaus, M. Radovic, M.J. Green, Adv. Mater. Interfaces 7 (2020) 2000845.
[54] X. Li, M. Li, Q. Yang, D. Wang, L. Ma, G. Liang, Z. Huang, B. Dong, Q. Huang, C. Zhi, Adv. Energy Mater. 10 (2020) 2001394.
[55] X. Li, M. Li, Q. Yang, G. Liang, Z. Huang, L. Ma, D. Wang, F. Mo, B. Dong, Q. Huang, C. Zhi, Adv. Energy Mater. 10 (2020) 2001791.
[56] Y. Song, T.-Y. Liu, X.-X. Xu, D.-Y. Feng, Y. Li, X.-X. Liu, Adv. Funct. Mater. 25 (2015) 4626–4632.
[57] T. Huang, S. Cai, H. Chen, Y. Jiang, S. Wang, C. Gao, J. Mater. Chem. A 5 (2017) 8255–8260.
[58] Z. Fan, Y. Wang, Z. Xie, D. Wang, Y. Yuan, H. Kang, B. Su, Z. Cheng, Y. Liu, Adv. Sci. 5 (2018) 1800750.